









Chiral phonons in the honeycomb sublattice of layered CoSn-like compounds

Andrzej Ptok ^{1,*}, Akxel Kobiałka ², Małgorzata Sternik ¹, Jan Łażewski ¹, Paweł T. Jochym ¹, Andrzej M. Oleś ^{3,4},
Svetoslav Stankov ^{5,6} and Przemysław Piekarz ^{1,†}

¹*Institute of Nuclear Physics, Polish Academy of Sciences, W. E. Radzikowskiego 152, PL-31342 Kraków, Poland*

²*Institute of Physics, Maria Curie-Skłodowska University, Plac Marii Skłodowskiej-Curie 1, PL-20031 Lublin, Poland*

³*Institute of Theoretical Physics, Jagiellonian University, Profesora Stanisława Łojasiewicza 11, PL-30348 Kraków, Poland*

⁴*Max Planck Institute for Solid State Research, Heisenbergstrasse 1, D-70569 Stuttgart, Germany*

⁵*Laboratory for Applications of Synchrotron Radiation, Karlsruhe Institute of Technology, D-76131 Karlsruhe, Germany*

⁶*Institute for Photon Science and Synchrotron Radiation, Karlsruhe Institute of Technology, D-76344 Eggenstein-Leopoldshafen, Germany*



(Received 8 June 2021; accepted 9 August 2021; published 20 August 2021)

Honeycomb and kagome lattices exhibit extraordinary electronic properties. It is a natural consequence of additional discrete degree of freedom associated with a valley or the occurrence of electronic flat bands. The combination of both types of lattices, observed in CoSn-like compounds, leads not only to the topological electronic behavior, but also to the emergence of chiral phonon modes. We study CoSn-like compounds and show that chiral phonons are realized here. Previous theoretical studies demonstrated that the chiral phonons can be found in ideal two-dimensional honeycomb or kagome lattices. Recent experimental results support such a prediction as the chiral phonons were observed in the transition metal dichalcogenide WSe_2 . It turns out that in the case of CoSn-like systems with the $P6/mmm$ symmetry, the kagome lattice formed by d -block element is decorated by the additional p -block atom. As a result one finds a two-dimensional triangular lattice of atoms with nonequal masses and the absence of chiral phonons in the kagome plane. Contrary to this, the interlayer honeycomb lattice of p -block atoms is preserved and allows for the realization of chiral phonons. In this paper we discuss the properties of such chiral phonons in seven CoSn-like compounds and demonstrate that they do not depend on the atomic mass ratio or the presence of intrinsic magnetic order. The chiral phonons of d -block atoms can be restored by removing the inversion symmetry. The latter is possible in the crystal structure of CoGe and RhPb with the reduced symmetry ($P\bar{6}2m$) and in distorted-kagome-like lattice.

DOI: [10.1103/PhysRevB.104.054305](https://doi.org/10.1103/PhysRevB.104.054305)

I. INTRODUCTION

Graphene—an exact, two-dimensional (2D) honeycomb lattice, exhibits a range of extraordinary electronic properties [1–6]. The existence of two degenerate and inequivalent valleys at the corners of the Brillouin zone (BZ) constitutes an additional discrete degree of freedom. This leads to a proposal of the *valleytronics* [7], which contrary to the spintronics concept [8], manipulates a valley index instead of carrier spin. Recently, the potential application in valleytronics for several three-dimensional (3D) systems (e.g., for transition metal dichalcogenides) has been suggested [9–11].

Due to the broken inversion symmetry of crystal structure, electrons in both valleys experience an effective magnetic field with equal magnitudes but opposite signs [12]. Such behavior, associated with effective angular momenta at the point with opposite valley indices, opens a way for optical pumping of valley-polarized carriers by circularly polarized light [13–17]. Additionally, new phenomena like valley Hall effect can be realized [18–21], which is analog to the spin Hall effect [22]. The mentioned transport properties exhibit a

topological nature, which is evidenced by the presence of the finite Berry curvature in the system [23–25].

Interestingly, electronic systems are not unique in containing such topological properties, as this is possible also for various types of bosonic systems [26,27]. The topological bosons are not an ordinary extension of the topological fermions due to significant difference between both systems (e.g., different types of statistics and interactions). However, from a theoretical point of view, both of them can be described by the Bloch wave function in periodic lattices [28]. The topological concepts widely used in electronic systems, such as Berry phase, Berry curvature, or Chern number, are applicable to bosonic systems as well.

As an example, a topologically nontrivial phase was observed in photonic systems [29–31]. Recently, many other topological features were reported in these types of systems, e.g., Weyl points [32–36], topological edge modes [30,36–38], or a topological acoustic wave in metamaterial systems [35,39–42]. Stemming from that, topological properties can be also expected in the case of phononic systems [43,44]. The topological properties of phonons can be a consequence of acoustic—and optical—mode inversion in phonon dispersion relations [45], which is an exact analog of the band inversion in the electronic structure. Consequently, also Dirac and/or Weyl points [46–59], as well as nodal lines [58–60], can occur.

* aptok@mmj.pl

† piekarz@wolf.ifj.edu.pl

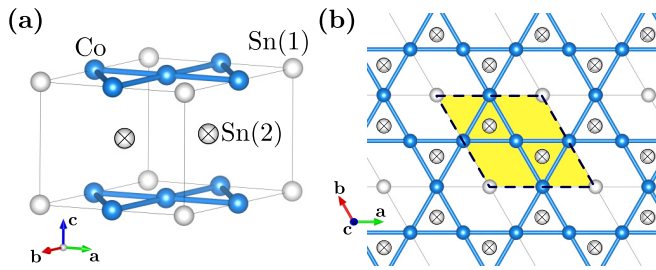


FIG. 1. (a) Side and (b) top view of the CoSn-like crystal structure with $P6/mmm$ symmetry. The Co atoms (blue balls) form the kagome lattice, while the Sn atoms occupy two nonequivalent positions: Sn(1) located in the plane of the kagome lattice (gray balls), and Sn(2) located between two kagome-lattice planes and forming a honeycomb sublattice (crossed balls).

One of the possible examples where phonons exhibit topological properties are chiral modes [61], associated with circular motion of atoms during mode propagation. These types of vibrations are characterized by the opposite chirality and can emerge in the system due to the quantized Berry phase and pseudoangular momenta [62–64]. In analogy to the electronic structure of graphene, in the phonon spectrum of the hexagonal lattice the opposite Berry phase in the K and K' points are observed [46,64–66]. The existence of chiral phonons allows for the realization of the elastic analog of the valley Hall effect [67]. Chiral phonons have been reported also in the kagome lattice [68], in the bilayer triangular [69], or bilayer hexagonal [70] lattices. Such type of phonons was also recently observed in the transition metal dichalcogenide WSe_2 [71] and predicted to exist in a MoS_2/WS_2 heterostructure [72]. In addition, recent studies show the possibility of experimental realization of the chiral phonons in more complex systems like BiB_3O_6 [73]. Recent studies considered various mechanisms that allow for phonons to gain angular momentum, e.g., laser pumping [74], magnetic field [75], temperature gradients [76], and electric fields [77,78]. Thereby, the chiral phonons can exhibit magnetic moments [75,79–81], which can play a role in the manipulation of phonons through external magnetic field.

Motivation. Several groups of 3D crystals can combine into two different types of 2D topological lattices. One such example is the structure of CoSn-like compounds [cf. Fig. 1(a)], formed by d -block element (like Fe, Co, Ni, Rh, or Pt) and p -block element (like Ge, In, Sn, Tl, or Pb). These compounds crystallize within the $P6/mmm$ symmetry—the d -block elements form a kagome sublattice, while the p -block elements have two nonequivalent positions: one position in the plane of the kagome lattice, and the second intercalated between two kagome-lattice planes [marked in Fig. 1 as Sn(1) and Sn(2), respectively]. Atoms in an Sn(2)-type position form the honeycomb sublattice [atoms marked by cross in Fig. 1(b)]. This complex structure arises due to the existence of the kagome lattice and allows for a realization of topological nearly flat band in electronic band structure [82,83].

In our study we investigate the following compounds: CoSn, CoGe, FeSn, FeGe, NiIn, RhPb, and PtTl. These materials permit a systematic study of the impact of various parameters, e.g., atomic mass ratio or magnetic order on the

chiral phonons in real 3D systems. Note that the application of an external uniaxial pressure on the system can mimic the effective magnetic field or the spin-orbit couplinglike effects acting on phonons. Furthermore, we found that two of the investigated compounds (i.e., CoGe and RhPb) cannot exist in the $P6/mmm$ structure. Instead they exhibit $P\bar{6}2m$ symmetry, which was not reported previously in literature. Our results suggests a possible emergence of chiral phonon also in these structures. Summarizing, we systematically study and discuss the origin of the chiral phonons in a large class of real 3D systems.

The paper is organized as follows. Details of the *ab initio* calculations are presented in Sec. II. Next, in Sec. III we discuss the numerical results. Possible experimental consequences of the realization of chiral phonons are discussed in Sec. IV. Finally, a summary is included in Sec. V.

II. THEORETICAL BACKGROUND

A. Numerical calculation details

The first-principles density functional theory (DFT) calculations are performed using the projector augmented-wave (PAW) potentials [84] implemented in the Vienna *ab initio* simulation package (VASP) code [85–87]. The calculations are made within generalized gradient approximation (GGA) in the Perdew, Burke, and Ernzerhof (PBE) parametrization [88]. The energy cutoff for the plane-wave expansion was set to 350 eV. The calculations carried out without and with spin polarization in a system with different spin configurations allow us to determine the magnetic ground state. Optimizations of the structural parameters (lattice constants and atomic positions) for nonmagnetic and ferromagnetic (FM) order are performed in the primitive unit cell using $10 \times 10 \times 6$ \mathbf{k} -point grid in the Monkhorst-Pack scheme [89]. For the antiferromagnetic (AFM) structure the doubled unit cell and the reduced \mathbf{k} -point grid ($10 \times 10 \times 3$) was used. As a convergence condition of the optimization loop, we take the energy difference of 10^{-5} and 10^{-7} eV for ionic and electronic degrees of freedom.

The interatomic force constants (IFC) are calculated with ALAMODE software [90], using the $2 \times 2 \times 2$ supercell with 48 atoms. Calculations are performed for the thermal distribution of multidisplacement of atoms at $T = 50$ K, generated within HECSS procedure [91]. The energy and the Hellmann-Feynman forces acting on all atoms are calculated with VASP for 100 different configurations of atomic displacements in the supercell. In dynamical properties calculations we include first- and second-order phonon contributions, which correspond to harmonic and cubic IFC, respectively.

B. Dynamical matrix and polarization vector

The lattice dynamics of the system can be studied using the dynamical matrix:

$$D_{\alpha\beta}^{jj'}(\mathbf{q}) \equiv \frac{1}{\sqrt{m_j m_{j'}}} \sum_n \Phi_{\alpha\beta}(j0, j'n) \exp(i\mathbf{q} \cdot \mathbf{R}_{jn}), \quad (1)$$

where \mathbf{q} is the phonon wave vector and m_j denotes the mass of j th atom. Here $\Phi_{\alpha\beta}(j0, j'n)$ is the IFC tensor (α and β denotes the direction index, i.e., x , y , and z) between j th and

j' th atoms located in the initial (0) and n th primitive unit cell. The phonon spectrum for a given wave vector \mathbf{q} is specified by the eigenproblem of the dynamical matrix (1), i.e.,

$$\omega_{\varepsilon\mathbf{q}}^2 \mathbf{e}_{\varepsilon\mathbf{q}\alpha j} = \sum_{j'\beta} D_{\alpha\beta}^{jj'}(\mathbf{q}) \mathbf{e}_{\varepsilon\mathbf{q}\beta j'}. \quad (2)$$

Here the ε branch describes the phonon with $\omega_{\varepsilon\mathbf{q}}$ frequency and polarization vector $\mathbf{e}_{\varepsilon\mathbf{q}\alpha j}$. Each αj component of the polarization vector denotes displacement of the j th atom in the α th direction.

C. Circular phonon polarization

In practice, the polarization vector $\mathbf{e}_{\varepsilon\mathbf{q}\alpha j}$ is related to the oscillation of each atom caused by the propagation of an ε phonon with a wave vector \mathbf{q} . Oscillations of each j th atom are described by three components of $\mathbf{e}_{\varepsilon\mathbf{q}\alpha j}$, which refer to oscillations in each of $\alpha \in \{x, y, z\}$ directions. The circular polarization occurs when the two orthogonal oscillators are of equal magnitude and are out of phase by exactly $\pm\pi/2$. To study this behavior we performed theoretical analysis of the polarization vectors, analogically to the previous study [64].

First, we employ Jones vectors $\frac{1}{\sqrt{2}}(1 \pm i)^T$ (denoting circular polarization in the xy plane), where upper and lower sign correspond to left-handed polarization (LHP) and right-handed polarization (RHP), respectively. From the theoretical point of view, Jones vectors act on every j th atom, and can be used to introduce a new basis defined as: $|R_j\rangle \equiv \frac{1}{\sqrt{2}}(1 \ i \ 0 \cdots 0)^T$, $|L_j\rangle \equiv \frac{1}{\sqrt{2}}(1 \ -i \ 0 \cdots 0)^T$, $|Z_j\rangle \equiv (0 \ 0 \ 1 \cdots 0)^T$; ...; $|R_j\rangle \equiv \frac{1}{\sqrt{2}}(0 \cdots 1 \ i \ 0 \cdots 0)^T$, $|L_j\rangle \equiv \frac{1}{\sqrt{2}}(0 \cdots 1 \ -i \ 0 \cdots 0)^T$, $|Z_j\rangle \equiv (0 \cdots 0 \ 0 \ 1 \ \cdots 0)^T$; ...; i.e., two in-plane components of circular oscillation are replaced by the Jones vectors coefficients, while the third component is unchanged. In this basis, each polarization vector $\mathbf{e} \equiv \mathbf{e}_{\varepsilon\mathbf{q}\alpha j}$, can be represented as

$$\mathbf{e} = \sum_j (\alpha_j^R |R_j\rangle + \alpha_j^L |L_j\rangle + \alpha_j^Z |Z_j\rangle), \quad (3)$$

where $\alpha_j^V = \langle V_j | \mathbf{e} \rangle$, for $V \in \{R, L, Z\}$ and $j \in \{1, 2, \dots, N\}$ (N is a total number of atoms in a primitive unit cell). Additionally we can define the phonon circular polarization operator \hat{S}_{ph}^z along the z direction as

$$\hat{S}_{\text{ph}}^z \equiv \sum_j \hat{S}_j^z = \sum_j (|R_j\rangle \langle R_j| - |L_j\rangle \langle L_j|), \quad (4)$$

where \hat{S}_i^z is the phonon circular polarization operator at site i . From this, the phonon circular polarization s_j^z of the j th atom can be expressed as

$$s_j^z = \hbar \mathbf{e}^\dagger \hat{S}_j^z \mathbf{e} = \hbar (|\alpha_j^R|^2 - |\alpha_j^L|^2). \quad (5)$$

It corresponds to the phonon angular momentum along the z direction [62,92]. However, in the general case, we can discuss the angular momenta along some arbitrary direction. For $s_j^z > 0$ ($s_j^z < 0$) the phonon mode has RHP (LHP), while for $s_j^z = 0$ the phonon mode is linearly polarized. Finally, the total phonon circular polarization $s_{\text{ph}}^z = \sum_j s_j^z$ denotes polarization of a whole system.

TABLE I. Comparison of the experimental and theoretical lattice constants for crystals in $P6/mmm$ symmetry. The results are obtained in the presence of spin-orbit coupling. Θ denotes the mass ratio of components, i.e., the relation of the mass of d -block element with respect to the mass of p -block element.

	Θ (-)	Theory		Expt. [82]	
		a (Å)	c (Å)	a (Å)	c (Å)
<i>P6/mmm</i> (SG: 191)					
CoSn	0.50	5.289	4.224	5.2693	4.2431
CoGe ^a	0.81	4.987	3.876	–	–
FeSn ^b	0.47	5.285	4.456	5.2765	4.4443
FeGe ^c	0.77	4.963	4.063	4.9852	4.0482
NiIn	0.51	5.280	4.377	5.2296	4.3390
RhPb ^a	0.49	5.740	4.487	5.6660	4.4127
PtTl	0.96	5.702	4.797	5.6017	4.6276
<i>P6̄2m</i> (SG: 189)					
CoGe	0.81	5.009	3.857	–	–
RhPb	0.49	5.770	4.464	–	–

^aUnstable in $P6/mmm$ structure, cf. discussion in Sec. III.

^bAFM order.

^cFM order.

III. RESULTS AND DISCUSSION

A. Crystal structure

The CoSn-like compounds typically crystallize in the hexagonal structure with $P6/mmm$ symmetry (space group: 191). The d -block element is placed at $3f$ ($1/2, 0, 0$) Wyckoff position, while the p -block atoms occupy two nonequivalent $1a$ ($0, 0, 0$) and $2d$ ($1/3, 2/3, 1/2$) Wyckoff positions.

Lattice parameters of the optimized ground-state structures are summarized in Table I. As shown, they remain in close agreement with the available experimental data. Two of the seven studied compounds have been previously reported to be magnetically ordered. The magnetic moments on Fe atoms are aligned ferromagnetically in FeGe [93,94], while in FeSn the AFM order is observed [95]. In AFM structure the spins are arranged ferromagnetically in each FeSn layer and antiferromagnetically ordered in neighboring layers.

For all compounds with the $P6/mmm$ symmetry, the phonon dispersion relations are calculated and presented in Fig. 2. The irreducible representations at the Γ point are: $A_{2u} + E_{1u}$ for acoustic modes, and $2A_{2u} + B_{1g} + B_{1u} + B_{2u} + E_{2u} + E_{2g} + 3E_{1u}$ for optic modes. The phonon dispersions are discussed in details in Sec. III B, but here we would like to point out that two crystals, CoGe and RhPb, are not stable in the $P6/mmm$ structure because their phonon spectra exhibit imaginary frequencies. From analysis of the soft mode with the lowest frequency (at the Γ point), we found a stable structure for these two compounds, i.e., the $P6̄2m$ hexagonal symmetry (space group 189), for details see Sec. III C. For both materials, the lattice constants of a new structure remain almost unchanged (Table I), however, the d -block element is slightly shifted from the original high-symmetry site ($0.5, 0, 0$) in the $P6/mmm$ structure to new $3f$ positions of a $P6̄2m$ space group, ($0.4665, 0, 0$) or ($0.4669, 0, 0$) for Co or Rh, respectively.

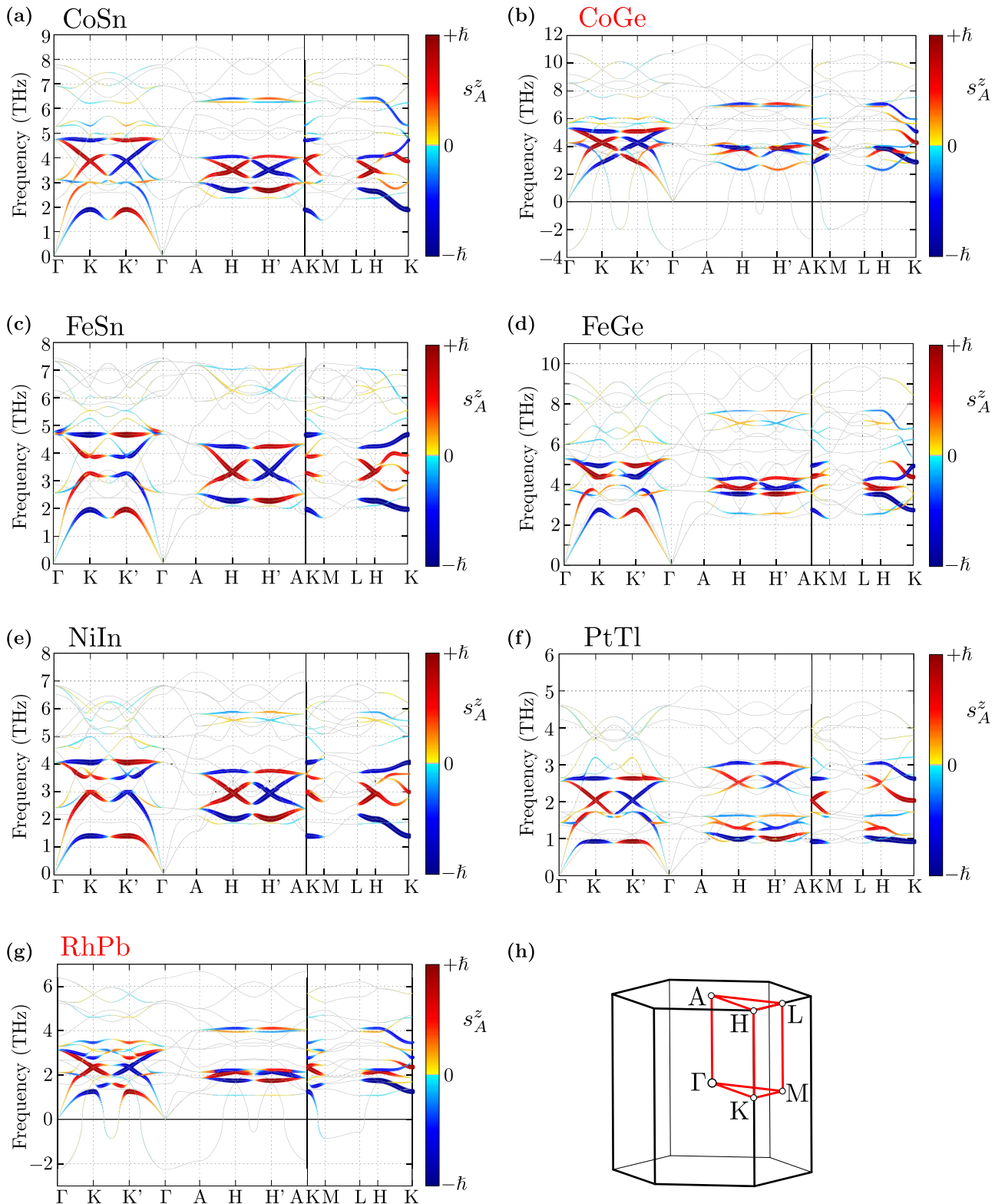


FIG. 2. (a)–(g) The phonon dispersions for the studied compounds (as labeled), along the high symmetry points of the first Brillouin zone, presented in (h), of the $P6/mmm$ structure. The color and width of line correspond to the phonon angular momentum of the p -block element in sublattice A of the honeycomb net (cf. Fig. 3). Atoms in sublattice B are described by the phonon angular momentum with the opposite value. Red labels denotes the compounds unstable in the $P6/mmm$ structure.

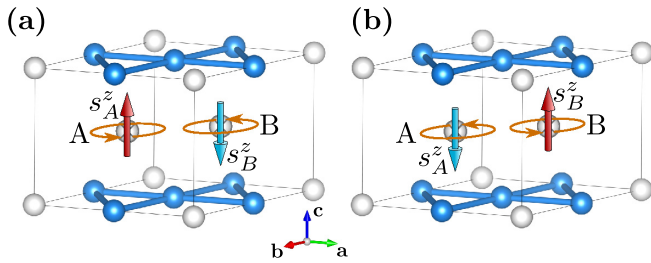


FIG. 3. The phonons angular momentum in two nonequivalent sites of the honeycomb net for the $P6/mmm$ structure. The p -block elements located on sites A and B of the honeycomb net have the opposite phonon angular momenta.

B. Chiral phonons in $P6/mmm$ symmetry

The phonon dispersion relations of the studied compounds are presented in Fig. 2. Each compound exhibits phonon flat bands, which can be connected with the collective atomic vibrations in the kagome-sublattice plane [96]. However, the analysis of the phonon angular momentum (phonon dispersion curves distinguished by colors and width of lines in Fig. 2, shows that these bands are mostly associated with chiral phonons involving the p -block elements within the honeycomb sublattice (see movies `k_mode*` in the Supplemental Material (SM) [97]). Two atoms composing this sublattice, exhibit an opposite phonon angular momentum, which is schematically presented in Fig. 3. For example, when the atom located at the A site has $s_A^z = \pm\hbar$, the atom at the B site has $s_B^z = \mp\hbar$.

Interestingly, chiral modes preserve the time reversal symmetry (s_j^z, \mathbf{k}) \rightarrow ($-s_j^z, -\mathbf{k}$), i.e., for K and K' points of the reciprocal space, since the components of polarization vectors for each atom correspond to opposite phonon angular momenta as it is depicted on the left panel for K and right panel for K' of Fig. 3. Along the path from K to K' point, the phonon angular momentum changes its value continuously and equals to zero at point M (i.e., precisely halfway between K and K'). Similarly, the phonon angular momentum also vanishes at the Γ point.

As we can see in Fig. 2, the phonon branches with strong phonon angular momentum (marked by thick lines), are located mostly in the mid-frequency range and emerge from the double-degenerate E_{1u} modes at the Γ point. Moving away from the Γ point these modes become nondegenerate and lead to the creation of circularlike rotation of p -block elements in the honeycomb lattice (this also happens at the Γ point, however, in this case circular polarization results from the composition of two double-degenerate E_{1u} or E_{2g} modes).

In the high-frequency range of the spectrum, a small but nonzero phonon angular momentum is also observed. These modes correspond to oscillations in the kagome layer, which also indirectly affect the honeycomb sublattice. Some examples of atom trajectories generated by the selected modes are shown in Fig. 4. When the phonon angular momentum is relatively large (approximately equal to a nominal value $\pm\hbar$), the p -block atoms realize a full circular movement with a small contribution from atoms in the kagome layer [e.g., Fig. 4(a)]. On the other hand, a small value of the angular mo-

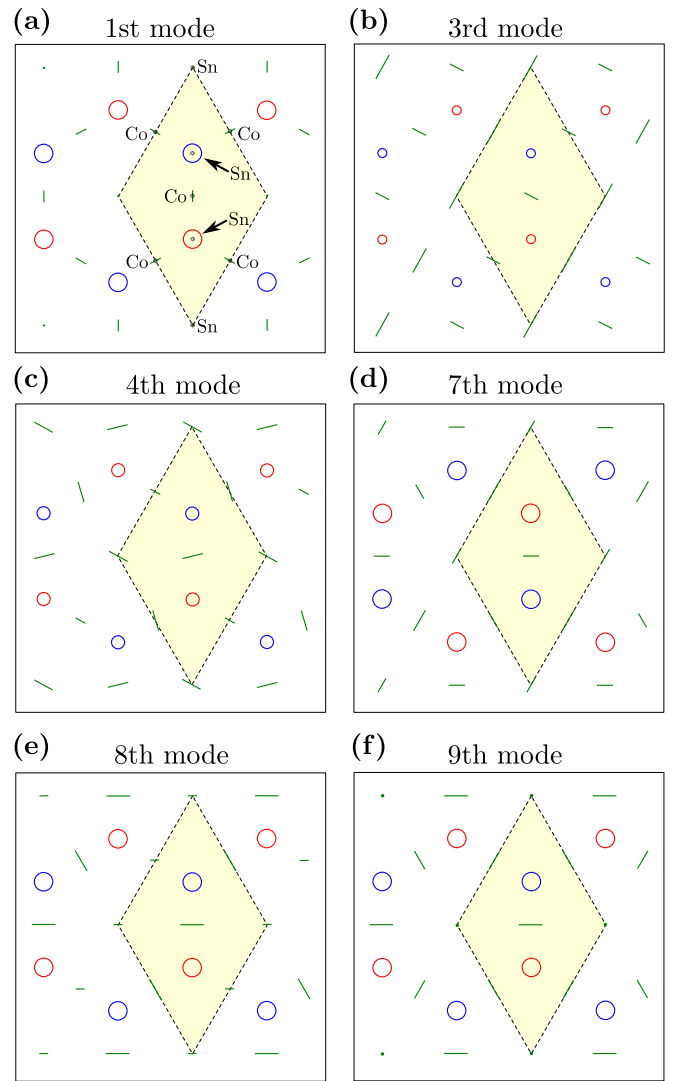


FIG. 4. Examples of trajectories (solid lines) of the CoSn atoms (for $P6/mmm$ symmetry), generated by selected modes at the K point (as labeled). The dashed yellow rhombus represents the unit cell, while equilibrium position of atoms are marked by dots in (a). The black arrows indicate the Sn atoms belonging to the honeycomb lattice and show its chiral vibrations. Red and blue circles correspond to the chiral modes with left-handed and right-handed polarization, respectively.

mentum (much smaller than the nominal value), corresponds to a small circular [e.g., Fig. 4(b)] or ellipticlike oscillations, and also affects d -block atoms (realizing linear oscillation). Movies visualizing the presented trajectories are included in the SM [97].

The chiral phonons are not observed in the kagome layer of the d -block atoms. In fact, this layer is composed of the kagome sublattice and one p -block atom forming together a two-dimensional triangular lattice of atoms with nonequal masses. Nevertheless, the p -block atoms within the honeycomb net can form a circular movement with relatively “small” nonzero phonon angular momentum, even if the modes propagate within the kagome layer. These features are clearly visible in the case of high-frequency modes

propagating with wave vectors H or H' (see Fig. 2). In such a case, the observed modes involve mostly vibration of d -block atoms with a small contribution of p -block atoms vibration.

Phonon dispersion relations exhibit also nodal lines (degenerate along the K - H and K' - H' paths), permitted by the C_{3v} symmetry element of the discussed space group [98]. Some of these nodal lines are composed of degenerate branches with strong phonon angular momentum (characteristic blue or red X-cut of two branches at K or K' point). This suggests the possibility for the realization of a phonon ballistic transport in certain situations.

The chiral modes appear in each studied system, but their frequencies depend strongly on the atomic composition of the compound. To describe the interplay between the modes with nonzero chirality and other vibrations, the phonon density of states (DOS) and the atom-projected partial DOS spectra, shown in Fig. 5, should be discussed together with the phonon dispersion relations (Fig. 2). The contributions of the vibrations of p -block and d -block atoms to the total DOS are mainly related to the mass ratio between atoms (cf. Table I).

In the case of systems with a large mass difference, these partial DOSs are well separated, as it is seen for CoSn, FeSn, NiIn, and RhPb, where the phonon modes of p -block (d -block) atoms are located at the lower (higher) frequencies. In the case of nearly equal masses (e.g., PtTi), phonons cover the same frequency regions. The chiral modes contribute to the partial DOS of the p -block atoms in the honeycomb sublattice (marked in blue). These modes can be derived from local minima and maxima of phonon dispersion relations at the high symmetry points (mostly at K , K' , and M or related H , H' , and L ; see Fig. 2), and are connected to the chiral modes propagating along the c direction. In the low frequency range, comprising the lowest chiral mode branch, small peaks in DOS corresponding to the chiral modes are observed. However, they are not dominating components of DOS. The main contribution of chiral modes is observed in the mid-frequency range, where several peaks related to the Van Hove singularities are located. In this part, the vibrations of atoms in a honeycomb sublattice dominate, however they are often mixed with the vibrations of other atoms. The flat bands (between K - K' or H - H' points) are also reflected in the DOS in the form of clearly visible peaks. A good example is the low-energy flat band corresponding to the vibrations of p -block atoms in the kagome plane. For instance, the distinct peak about 1.75 THz in Fig. 5(e).

Unlike the ab plane, the phonon branches preserve chirality along the c direction (which corresponds to the unchanged color of the line between K and H points in Fig. 2). Each wave vector along this path corresponds to the propagation of a chiral mode along the c direction—due to the conservation of angular momentum rule [99], the mode should be “topologically” protected. If the sample thickness will be smaller than the phonon scattering length but larger than the electron scattering length, the chirality information should not be lost during the propagation [100]. In this sense, the chiral modes represent a key step toward utilizing chiral phonons in quantum devices [43].

Now we shortly discuss the origin of the chiral phonons in a general case, and in the context of their microscopic

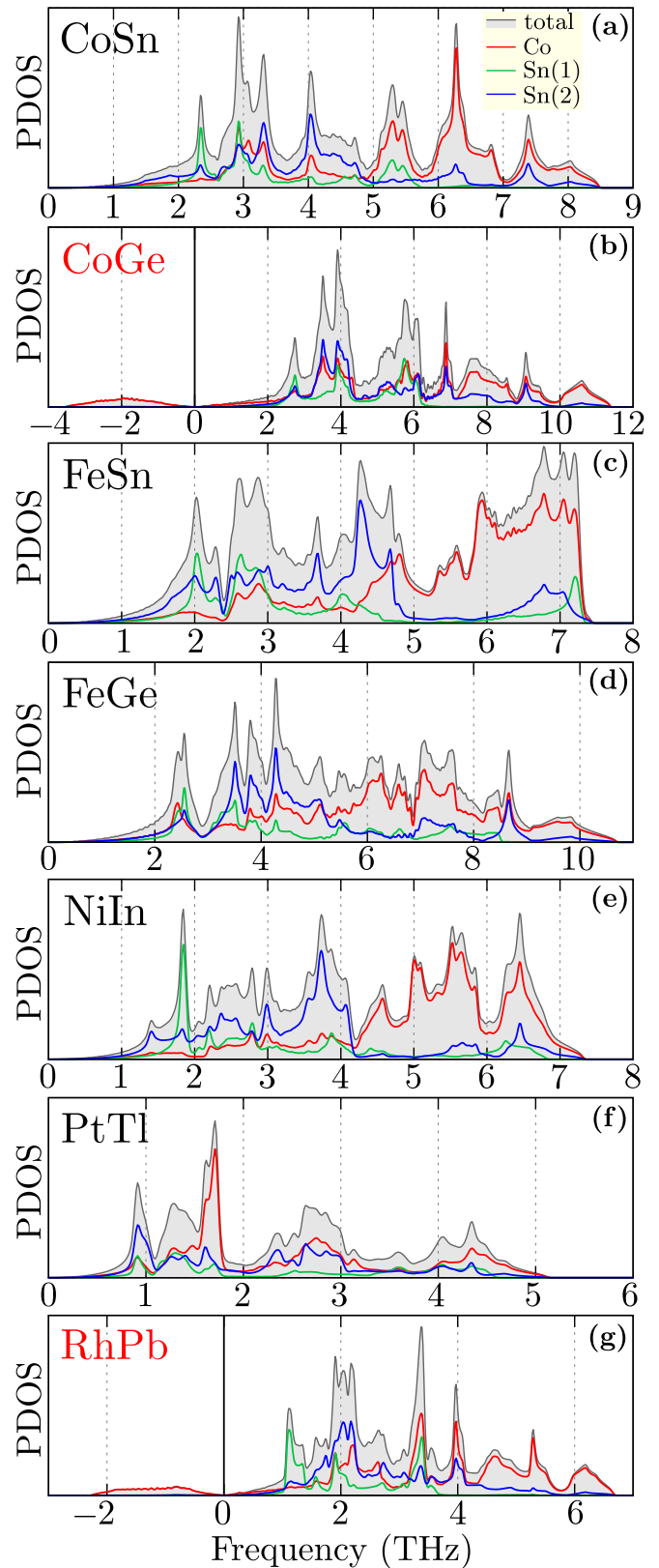


FIG. 5. The total and partial phonon density of states (PDOS) for the studied compounds (as labeled) of the $P6/mmm$ structure. The filled gray area corresponds to the total DOS, while red, green, and blue lines denote the partial DOS for d -block element (kagome sublattice), p -block element in kagome plane [position Sn(1) in Fig. 1], and p -block elements in the honeycomb sublattice [position Sn(2) in Fig. 1], respectively.

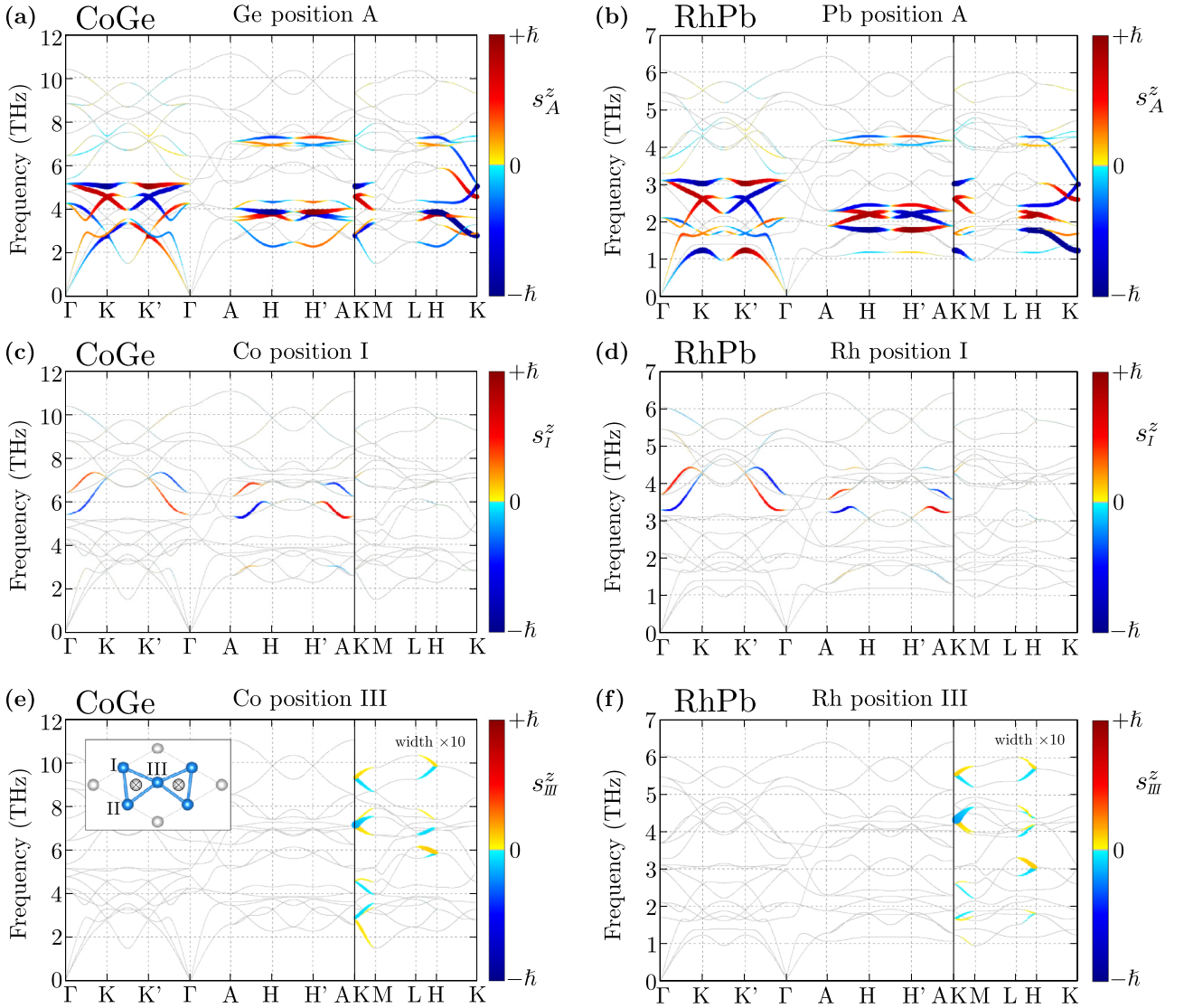


FIG. 6. Phonon dispersions of CoGe and RhPb in the stable $P\bar{6}2m$ structure. Panels from top to bottom represent the phonon angular momentum of the p -block element in the A sublattice of the honeycomb net (cf. Fig. 3), and the d -block atoms in position I and III [see inset in (e) presenting the position of the d -block atoms in distorted-kagome lattice]. At bottom panels, the widths of lines are magnified 10 times. Meaning of colors and width of lines is the same as in Fig. 2.

sources [101]. Let us start from the discussion of a general case. The lattice dynamics of a system depends on the IFC matrix (including first- and high-order phonon contributions). In the case of a system with the inversion symmetry, the first-order IFC are highly symmetric. Similarly, when the inversion symmetry is broken, then this breaking will affect the first-order IFC matrix. In this situation, some components of IFC are nonequal under mirror symmetry due to different neighborhoods of certain lattice sites. As a result, the phonon modes will have angular momentum at a nonsymmetric point in the Brillouin zone (e.g., such a situation was observed in dichalcogenides [71,72]). Moreover, the higher-order IFC can play a role in the realization of chiral phonons, especially in system with the broken time reversal (e.g., iron, cobalt, or nickel [102]).

In the case of CoSn-like compounds, the atoms are located at the high symmetry points, which implies inversion sym-

metry. In fact, the source of the chiral phonons is “coded” in the first-order IFC preserved by a threefold axis (along the z direction) of the honeycomb sublattice, while the total phonon angular momentum of the system is equal to zero [101]. Note that in magnetic compounds like FeSn and FeGe, the time reversal symmetry can be broken by the magnetic moment of iron. However, the chiral modes are not realized in the layer with d elements, due to the triangular lattice.

C. CoGe and RhPb in $P\bar{6}2m$ symmetry

Our analysis of the systems with the $P6/mmm$ symmetry revealed the soft modes in the phonon dispersion relations of CoGe and RhPb [cf. Figs. 2(b) and 2(g), respectively]. Thus, both structures are unstable and can be transformed to a distorted structure due to the condensation of the soft phonon mode. It means that using the displacement pattern attributed to the polarization vectors of this mode, the stable

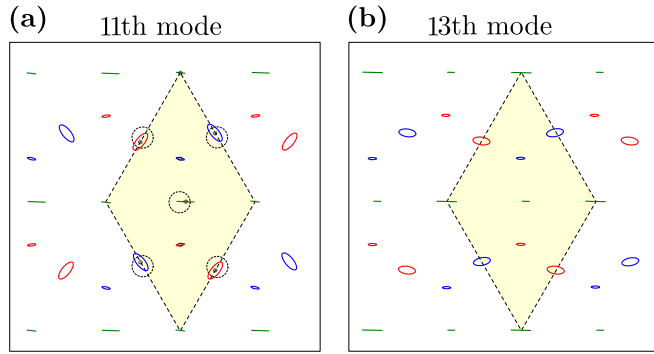


FIG. 7. Examples of trajectories (solid lines) of the CoGe atoms (for $P\bar{6}2m$ symmetry), generated by chosen modes at the $K/3$ point (as labeled). The dashed yellow rhombus represents the unit cell, while positions of atoms are the same as in Fig. 4. Here the gray dashed circles in (a) correspond to positions of sites in the ideal kagome lattice. The meaning of the colored lines is the same as in Fig. 4.

lower-symmetry configurations can be found. For CoGe and RhPb, the lowest frequency soft modes at the Γ point with B_{1u} symmetry consist of specific displacements of d elements only.

In practice, the triangles constructing the kagome net in $P6/mmm$ crystals rotate approximately by 6° in opposite directions (see movie `gamma_mode4` in the SM [97]). This soft-mode-induced modification stabilizes both systems in the $P\bar{6}2m$ symmetry. In fact, in the case of RhPb, the lattice constants for the $P6/mmm$ and $P\bar{6}2m$ symmetries are comparable (cf. Table I), and in both cases they reproduce relatively well the experimental values [82].

Independently of the positions of d elements in the $P\bar{6}2m$ structure, the honeycomb net of p element remains unchanged and still exhibits the chiral phonons (top panels in Fig. 6). The main properties of the chiral phonon branches are similar to those observed in systems with the $P6/mmm$ symmetry [cf. Figs. 2(b) and 2(g)]. However, as a consequence of the kagome lattice distortion [see the inset in Fig. 6(e)], the inversion symmetry of the system is lost. As we discussed in Sec. III B, in such a case the chiral phonons can be expected also in this kagomelike sublattice. Indeed, the analysis of the phonon angular momentum for d -element atoms clearly reveals the existence of the chiral modes also in the distorted-kagome lattice. Interestingly, the chiral modes in this layer are realized only by d -element atoms, while one p -element atom shows the ordinary linear movement.

In addition, the d -element atoms move and form an ellipsoidal pattern (see Fig. 7) giving the phonon angular momentum smaller than the nominal. What is also interesting, the atoms at sites I and II have an antisymmetric position with respect to the p -element atom in the corner of the unit cell [rhombus in the inset of Fig. 6(e)]. As a consequence, similar to the honeycomb sublattice, the atoms in these positions have opposite phonon angular momenta. Also, the atom at position III exhibits in some branches the nonzero angular momentum (bottom panels in Fig. 6). Nevertheless, the total angular momentum of the distorted kagome lattice is equal to zero.

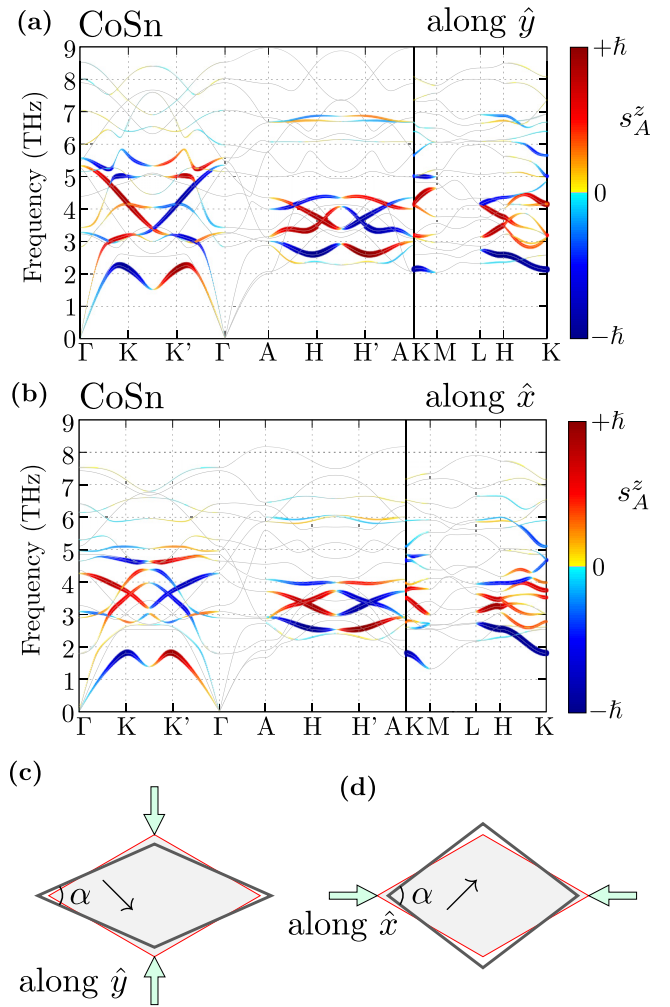


FIG. 8. Phonon dispersions of CoSn under uniaxial strain along the \hat{y} and \hat{x} direction, presented in (a) and (c), or (b) and (d), respectively. The meaning of colors and width of lines are the same as in Fig. 2.

D. Influence of uniaxial stress

We also examined the effect of the uniaxial stress applied along \hat{x} and \hat{y} directions (Fig. 8). Independently of the stress direction, the system symmetry changes from $P6/mmm$ to $Cmmm$ [mostly due to the modification of the angle between lattice vectors a and b —cf. Figs. 8(c) and 8(d)]. The first observed consequence is the modification of the degeneracy at the Γ point. Second, the crossing of the phonon branches is shifted from the BZ surface or a high symmetry point to the interior of the BZ. What is more, the initially flat bands change their curvature. Notably, the main features associated with the chiral phonons survive unchanged [cf. Figs. 2(a) and 8].

Effects induced by the uniaxial stress are similar to those resulting from the magnetic field and spin-orbit coupling modifying the electronic band structure. In the former case, points which were initially degenerate at the Γ point become decoupled. A similar effect was observed in the case of acoustic waves [103]. Lifting of the degeneracy leads to the emergence of the chiral phonons at k points close to the Γ point and can be useful for potential experimental detection, e.g., by circularly polarized Raman scattering [104] (cf. Sec. IV). In

addition, the mixing of the branches around K and K' is observed, which should correspond to the changes induced by the finite spin-orbit coupling, in analogy to the electronic systems.

IV. PROPOSED EXPERIMENTAL DETECTION

As we mentioned above, the chiral phonons in the case of $P6/mmm$ crystals are realized mostly within the honeycomb sublattice and are composed of p -element atoms in $2d$ Wyckoff position. For these positions, we can find two infrared (IR) active modes A_{2u} and E_{1u} as well as one Raman active mode E_{2g} . Consequently, chiral modes could be measured in a relatively simple way by IR or Raman spectroscopy. The realization of chiral phonons at k points in the close neighborhood of the Γ point under uniaxial pressure allows for performing the mentioned experiments. The circularly polarized Raman scattering of the real system can give some information about the chiral phonon frequencies at the Γ point.

The interaction with electromagnetic waves provides additional opportunities in experimental studies: A phonon with nonzero angular momentum can be created by emission or absorption of a photon with a given circular polarization [64,100]. During this process, the intervalley electron scattering at valley centers involving a valley center phonon is expected [71]. However, to improve the description of these processes, a study of the valley structure in electronic bands is needed, which is beyond the scope of this paper. We remark that in this type of studies, the circularly polarized Raman spectroscopy can be employed—this allows for the helically resolved spectroscopy and to study modes with different types of chirality. Indeed, these types of measurements have been successfully used for observation of the chiral phonon modes in a monolayer of the transition metal dichalcogenide WS_2 [105].

Recent theoretical analyses suggest the phononic-to-electronic conversion of angular momentum [106,107]. For example, the phonon angular momentum of the surface acoustic wave can control the magnetization of a FM layer, as shown in the case of Ni film in the Ni/LiNbO₃ hybrid device [108]. Similarly, the external magnetic field can lead to the decoupling of the frequencies of the initially degenerate modes [109]. Moreover, more recent studies suggest the existence of this behavior in magnetic systems concerning chiral phonons [110]. In such a way, the modification of the phonon spectra at the Γ point under external magnetic field should be observed. Equivalently, the uniaxial pressure can be applied resulting in a similar effect (as discussed in Sec. III D).

The appearance of a nonzero phonon angular momentum in the honeycomb sublattice of CoSn-like compounds, can be interesting also from the experimental point of view. Similarly to the electronic systems [111], in a properly prepared sample

(in slab form), phononic angular momentum Hall effect could be realized [112] (in analogy to the integer quantum Hall effect). Congenial effect was predicted for the photonic chiral edge state propagating along a surface [113]. Excitation of the edge mode with well-defined chirality can be induced by photons with the same circular polarization [114]. This effect could be measured as the occurrence of such edge modes should lead to the modification of the transport properties of such systems [12].

V. SUMMARY

Our study confirms that the ideal honeycomb [64] and kagome [68] lattices allow for the realization of chiral phonons (with nonzero angular momentum). Typically, the chiral phonons are observed in two-dimensional materials [61] and might serve as an interesting extension of the quantum devices based on phonons [43]. In this paper we discussed the realization of chiral phonons in the CoSn-like compounds—layered systems build by decorated kagome and honeycomb lattices. We demonstrated that the realization of an ideal honeycomb lattice by the p -block elements allows for the emergence of chiral phonons within this sublattice. In our study of CoSn-like compounds, based on the first-principles method, we showed that the properties of the chiral phonons do not depend on the mass ratio of constituent elements or on their intrinsic magnetic order.

Typically, CoSn-like compounds crystallize in the $P6/mmm$ structure. However, in two of the discussed compounds, i.e., in CoGe and RhPb, soft modes were revealed. We found that these soft modes lead to the stable $P6_2m$ structure. In this case, the absence of the inversion symmetry allows for the realization of the chiral modes also by the d -block atoms within the distorted-kagome sublattice. We remark that the symmetry of the system can be also changed by a uniaxial strain. The strain effect can mimic the magnetic field or spin-orbit coupling acting on phonons. Regardless of the modification of the symmetry, the main character of the chiral phonons remains unchanged. Additionally, we proposed an experimental method for the confirmation of the chiral phonons described here and found in CoSn-like compounds.

ACKNOWLEDGMENTS

Some figures and movies in this work were rendered using VESTA [115] and VMD [116] software. This work was supported by National Science Centre (NCN, Poland) under Projects No. 2016/21/D/ST3/03385 (A.P.), No. 2018/31/N/ST3/01746 (A.K.), No. 2016/23/B/ST3/00839 (A.M.O.), and No. 2017/25/B/ST3/02586 (P.P.). A.P. appreciates funding in the frame of scholarships of the Minister of Science and Higher Education (Poland) for outstanding young scientists (2019 edition, No. 818/STYP/14/2019).

[1] K. S. Novoselov, A. K. Geim, S. V. Morozov, D. Jiang, M. I. Katsnelson, I. V. Grigorieva, S. V. Dubonos, and A. A. Firsov, Two-dimensional gas of massless Dirac fermions in graphene, *Nature (London)* **438**, 197 (2005).

[2] A. H. Castro Neto, F. Guinea, N. M. R. Peres, K. S. Novoselov, and A. K. Geim, The electronic properties of graphene, *Rev. Mod. Phys.* **81**, 109 (2009).

[3] N. M. R. Peres, *Colloquium: The transport properties of graphene: An introduction*, *Rev. Mod. Phys.* **82**, 2673 (2010).

- [4] S. Das Sarma, S. Adam, E. H. Hwang, and E. Rossi, Electronic transport in two-dimensional graphene, *Rev. Mod. Phys.* **83**, 407 (2011).
- [5] M. O. Goerbig, Electronic properties of graphene in a strong magnetic field, *Rev. Mod. Phys.* **83**, 1193 (2011).
- [6] V. N. Kotov, B. Uchoa, V. M. Pereira, F. Guinea, and A. H. Castro Neto, Electron-electron interactions in graphene: Current status and perspectives, *Rev. Mod. Phys.* **84**, 1067 (2012).
- [7] F. Bussolotti, H. Kawai, Z. E. Ooi, V. Chellappan, D. Thian, A. L. C. Pang, and K. E. J. Goh, Roadmap on finding chiral valleys: screening 2D materials for valleytronics, *Nano Futures* **2**, 032001 (2018).
- [8] A. Avsar, H. Ochoa, F. Guinea, B. Özyilmaz, B. J. van Wees, and I. J. Vera-Marun, *Colloquium*: Spintronics in graphene and other two-dimensional materials, *Rev. Mod. Phys.* **92**, 021003 (2020).
- [9] J. R. Schaibley, H. Yu, G. Clark, P. Rivera, J. S. Ross, K. L. Seyler, W. Yao, and X. Xu, Valleytronics in 2D materials, *Nat. Rev. Mater.* **1**, 16055 (2016).
- [10] G. Wang, A. Chernikov, M. M. Glazov, T. F. Heinz, X. Marie, T. Amand, and B. Urbaszek, *Colloquium*: Excitons in atomically thin transition metal dichalcogenides, *Rev. Mod. Phys.* **90**, 021001 (2018).
- [11] Y. Liu, Y. Gao, S. Zhang, J. He, J. Yu, and Z. Liu, Valleytronics in transition metal dichalcogenides materials, *Nano Res.* **12**, 2695 (2019).
- [12] D. Xiao, W. Yao, and Q. Niu, Valley-Contrasting Physics in Graphene: Magnetic Moment and Topological Transport, *Phys. Rev. Lett.* **99**, 236809 (2007).
- [13] T. Cao, G. Wang, W. Han, H. Ye, C. Zhu, J. Shi, Q. Niu, P. Tan, E. Wang, B. Liu, and J. Feng, Valley-selective circular dichroism of monolayer molybdenum disulphide, *Nat. Commun.* **3**, 887 (2012).
- [14] K. F. Mak, K. He, J. Shan, and T. F. Heinz, Control of valley polarization in monolayer MoS₂ by optical helicity, *Nat. Nanotech.* **7**, 494 (2012).
- [15] G. Sallen, L. Bouet, X. Marie, G. Wang, C. R. Zhu, W. P. Han, Y. Lu, P. H. Tan, T. Amand, B. L. Liu, and B. Urbaszek, Robust optical emission polarization in MoS₂ monolayers through selective valley excitation, *Phys. Rev. B* **86**, 081301(R) (2012).
- [16] H. Zeng, J. Dai, W. Yao, D. Xiao, and X. Cui, Valley polarization in MoS₂ monolayers by optical pumping, *Nat. Nanotech.* **7**, 490 (2012).
- [17] S. Wu, J. S. Ross, G.-B. Liu, G. Aivazian, A. Jones, Z. Fei, W. Zhu, D. Xiao, W. Yao, D. Cobden, and X. Xu, Electrical tuning of valley magnetic moment through symmetry control in bilayer MoS₂, *Nat. Phys.* **9**, 149 (2013).
- [18] D. Xiao, G.-B. Liu, W. Feng, X. Xu, and W. Yao, Coupled Spin and Valley Physics in Monolayers of MoS₂ and Other Group-VI Dichalcogenides, *Phys. Rev. Lett.* **108**, 196802 (2012).
- [19] K. F. Mak, K. L. McGill, J. Park, and P. L. McEuen, The valley Hall effect in MoS₂ transistors, *Science* **344**, 1489 (2014).
- [20] W.-Y. Tong, S.-J. Gong, X. Wan, and C.-G. Duan, Concepts of ferrovalley material and anomalous valley Hall effect, *Nat. Commun.* **7**, 13612 (2016).
- [21] C. Jin, J. Kim, M. I. B. Utama, E. C. Regan, H. Kleemann, H. Cai, Y. Shen, M. J. Shinner, A. Sengupta, K. Watanabe, T. Taniguchi, S. Tongay, A. Zettl, and F. Wang, Imaging of pure spin-valley diffusion current in WS₂-WSe₂ heterostructures, *Science* **360**, 893 (2018).
- [22] J. Sinova, S. O. Valenzuela, J. Wunderlich, C. H. Back, and T. Jungwirth, Spin Hall effects, *Rev. Mod. Phys.* **87**, 1213 (2015).
- [23] D. Xiao, M.-C. Chang, and Q. Niu, Berry phase effects on electronic properties, *Rev. Mod. Phys.* **82**, 1959 (2010).
- [24] M. Z. Hasan and C. L. Kane, *Colloquium*: Topological insulators, *Rev. Mod. Phys.* **82**, 3045 (2010).
- [25] A. Bansil, H. Lin, and T. Das, *Colloquium*: Topological band theory, *Rev. Mod. Phys.* **88**, 021004 (2016).
- [26] Y. Liu, X. Chen, and Y. Xu, Topological phononics: From fundamental models to real materials, *Adv. Funct. Mater.* **30**, 1904784 (2020).
- [27] P. McClarty, Topological magnons: A review (2021), [arXiv:2106.01430](https://arxiv.org/abs/2106.01430).
- [28] F. Bloch, Über die quantenmechanik der elektronen in kristallgittern, *Z. Phys.* **52**, 555 (1929).
- [29] L. Lu, J. D. Joannopoulos, and M. Soljačić, Topological photonics, *Nat. Photonics* **8**, 821 (2014).
- [30] J. Noh, S. Huang, D. Leykam, Y. D. Chong, K. P. Chen, and M. C. Rechtsman, Experimental observation of optical Weyl points and Fermi arc-like surface states, *Nat. Phys.* **13**, 611 (2017).
- [31] T. Ozawa, H. M. Price, A. Amo, N. Goldman, M. Hafezi, L. Lu, M. C. Rechtsman, D. Schuster, J. Simon, O. Zilberberg, and I. Carusotto, Topological photonics, *Rev. Mod. Phys.* **91**, 015006 (2019).
- [32] L. Lu, L. Fu, J. D. Joannopoulos, and M. Soljačić, Weyl points and line nodes in gyroid photonic crystals, *Nat. Photonics* **7**, 294 (2013).
- [33] Q. Lin, M. Xiao, L. Yuan, and S. Fan, Photonic Weyl point in a two-dimensional resonator lattice with a synthetic frequency dimension, *Nat. Commun.* **7**, 13731 (2016).
- [34] J.-M. Hou and W. Chen, Weyl semimetals in optical lattices: moving and merging of Weyl points, and hidden symmetry at Weyl points, *Sci. Rep.* **6**, 33512 (2016).
- [35] H. He, C. Qiu, L. Ye, X. Cai, X. Fan, M. Ke, F. Zhang, and Z. Liu, Topological negative refraction of surface acoustic waves in a Weyl phononic crystal, *Nature (London)* **560**, 61 (2018).
- [36] W.-J. Chen, M. Xiao, and C. T. Chan, Photonic crystals possessing multiple Weyl points and the experimental observation of robust surface states, *Nat. Commun.* **7**, 13038 (2016).
- [37] X.-D. Chen, F.-L. Zhao, M. Chen, and J.-W. Dong, Valley-contrasting physics in all-dielectric photonic crystals: Orbital angular momentum and topological propagation, *Phys. Rev. B* **96**, 020202(R) (2017).
- [38] H. T. Phan, F. Liu, and K. Wakabayashi, Valley-dependent corner states in honeycomb photonic crystals without inversion symmetry, *Opt. Express* **29**, 18277 (2021).
- [39] Z. Yang, F. Gao, X. Shi, X. Lin, Z. Gao, Y. Chong, and B. Zhang, Topological Acoustics, *Phys. Rev. Lett.* **114**, 114301 (2015).
- [40] M. Xiao, W.-J. Chen, W.-Y. He, and C. T. Chan, Synthetic gauge flux and Weyl points in acoustic systems, *Nat. Phys.* **11**, 920 (2015).
- [41] J. Lu, C. Qiu, L. Ye, X. Fan, M. Ke, F. Zhang, and Z. Liu, Observation of topological valley transport of sound in sonic crystals, *Nat. Phys.* **13**, 369 (2017).

- [42] Z. Zhang, Y. Cheng, and X. Liu, Achieving acoustic topological valley-Hall states by modulating the subwavelength honeycomb lattice, *Sci. Rep.* **8**, 16784 (2018).
- [43] N. Li, J. Ren, L. Wang, G. Zhang, P. Hänggi, and B. Li, *Colloquium: Phononics: Manipulating heat flow with electronic analogs and beyond*, *Rev. Mod. Phys.* **84**, 1045 (2012).
- [44] J. Li, J. Liu, S. A. Baronett, M. Liu, L. Wang, R. Li, Y. Chen, D. Li, Q. Zhu, and X.-Q. Chen, Computation and data driven discovery of topological phononic materials, *Nat. Commun.* **12**, 1204 (2021).
- [45] S. Singh, Q. S. Wu, C. Yue, A. H. Romero, and A. A. Soluyanov, Topological phonons and thermoelectricity in triple-point metals, *Phys. Rev. Mater.* **2**, 114204 (2018).
- [46] Y. Jin, R. Wang, and H. Xu, Recipe for Dirac phonon states with a quantized valley Berry phase in two-dimensional hexagonal lattices, *Nano Lett.* **18**, 7755 (2018).
- [47] T. Zhang, Z. Song, A. Alexandradinata, H. Weng, C. Fang, L. Lu, and Z. Fang, Double-Weyl Phonons in Transition-Metal Monosilicides, *Phys. Rev. Lett.* **120**, 016401 (2018).
- [48] H. Miao, T. T. Zhang, L. Wang, D. Meyers, A. H. Said, Y. L. Wang, Y. G. Shi, H. M. Weng, Z. Fang, and M. P. M. Dean, Observation of Double Weyl Phonons in Parity-Breaking FeSi, *Phys. Rev. Lett.* **121**, 035302 (2018).
- [49] J. Li, Q. Xie, S. Ullah, R. Li, H. Ma, D. Li, Y. Li, and X.-Q. Chen, Coexistent three-component and two-component Weyl phonons in TiS, ZrSe, and HfTe, *Phys. Rev. B* **97**, 054305 (2018).
- [50] Q. Xie, J. Li, S. Ullah, R. Li, L. Wang, D. Li, Y. Li, S. Yunoki, and X.-Q. Chen, Phononic Weyl points and one-way topologically protected nontrivial phononic surface arc states in noncentrosymmetric WC-type materials, *Phys. Rev. B* **99**, 174306 (2019).
- [51] J. Liu, W. Hou, E. Wang, S. Zhang, J.-T. Sun, and S. Meng, Ideal type-II Weyl phonons in wurtzite CuI, *Phys. Rev. B* **100**, 081204(R) (2019).
- [52] M. Zhong, Y. Liu, F. Zhou, M. Kuang, T. Yang, X. Wang, and G. Zhang, Coexistence of phononic sixfold, fourfold, and threefold excitations in ternary antimonide $Zr_3Ni_3Sb_4$, *Phys. Rev. B* **104**, 085118 (2021).
- [53] Q.-B. Liu, Y. Qian, H.-H. Fu, and Z. Wang, Symmetry-enforced Weyl phonons, *npj Comput. Mater.* **6**, 95 (2020).
- [54] B. Peng, Y. Hu, S. Murakami, T. Zhang, and B. Monserrat, Topological phonons in oxide perovskites controlled by light, *Sci. Adv.* **6**, eabd1618 (2020).
- [55] Z. J. Chen, R. Wang, B. W. Xia, B. B. Zheng, Y. J. Jin, Y.-J. Zhao, and H. Xu, Three-Dimensional Dirac Phonons with Inversion Symmetry, *Phys. Rev. Lett.* **126**, 185301 (2021).
- [56] P.-F. Liu, J. Li, X.-H. Tu, H. Li, J. Zhang, P. Zhang, Q. Gao, and B.-T. Wang, First-principles prediction of ideal type-II Weyl phonons in wurtzite ZnSe, *Phys. Rev. B* **103**, 094306 (2021).
- [57] Q.-B. Liu, Z. Wang, and H.-H. Fu, Charge-four Weyl phonons, *Phys. Rev. B* **103**, L161303 (2021).
- [58] J. Li, Q. Xie, J. Liu, R. Li, M. Liu, L. Wang, D. Li, Y. Li, and X.-Q. Chen, Phononic Weyl nodal straight lines in MgB_2 , *Phys. Rev. B* **101**, 024301 (2020).
- [59] M. He, P. Rivera, D. Van Tuan, N. P. Wilson, M. Yang, T. Taniguchi, K. Watanabe, J. Yan, D. G. Mandrus, H. Yu, H. Dery, W. Yao, and X. Xu, Valley phonons and exciton complexes in a monolayer semiconductor, *Nat. Commun.* **11**, 618 (2020).
- [60] O. Stenull, C. L. Kane, and T. C. Lubensky, Topological Phonons and Weyl Lines in Three Dimensions, *Phys. Rev. Lett.* **117**, 068001 (2016).
- [61] H. Chen, W. Zhang, Q. Niu, and L. Zhang, Chiral phonons in two-dimensional materials, *2D Mater.* **6**, 012002 (2018).
- [62] L. Zhang and Q. Niu, Angular Momentum of Phonons and the Einstein-de Haas effect, *Phys. Rev. Lett.* **112**, 085503 (2014).
- [63] Y. Liu, C.-S. Lian, Y. Li, Y. Xu, and W. Duan, Pseudospins and Topological Effects of Phonons in a Kekulé Lattice, *Phys. Rev. Lett.* **119**, 255901 (2017).
- [64] L. Zhang and Q. Niu, Chiral Phonons at High-Symmetry Points in Monolayer Hexagonal Lattices, *Phys. Rev. Lett.* **115**, 115502 (2015).
- [65] Y. Liu, Y. Xu, and W. Duan, Berry phase and topological effects of phonons, *Natl. Sci. Rev.* **5**, 314 (2017).
- [66] J. Li, L. Wang, J. Liu, R. Li, Z. Zhang, and X.-Q. Chen, Topological phonons in graphene, *Phys. Rev. B* **101**, 081403(R) (2020).
- [67] R. K. Pal and M. Ruzzene, Edge waves in plates with resonators: An elastic analogue of the quantum valley Hall effect, *New J. Phys.* **19**, 025001 (2017).
- [68] H. Chen, W. Wu, S. A. Yang, X. Li, and L. Zhang, Chiral phonons in kagome lattices, *Phys. Rev. B* **100**, 094303 (2019).
- [69] X. Xu, W. Zhang, J. Wang, and L. Zhang, Topological chiral phonons in center-stacked bilayer triangle lattices, *J. Phys.: Condens. Matter* **30**, 225401 (2018).
- [70] M. Gao, W. Zhang, and L. Zhang, Nondegenerate chiral phonons in graphene/hexagonal boron nitride heterostructure from first-principles calculations, *Nano Lett.* **18**, 4424 (2018).
- [71] H. Zhu, J. Yi, M.-Y. Li, J. Xiao, L. Zhang, C.-W. Yang, R. A. Kaindl, L.-J. Li, Y. Wang, and X. Zhang, Observation of chiral phonons, *Science* **359**, 579 (2018).
- [72] W. Zhang, A. Srivastava, X. Li, and L. Zhang, Chiral phonons in the indirect optical transition of a MoS_2/WS_2 heterostructure, *Phys. Rev. B* **102**, 174301 (2020).
- [73] C. P. Romao, Anomalous thermal expansion and chiral phonons in BiB_3O_6 , *Phys. Rev. B* **100**, 060302(R) (2019).
- [74] T. F. Nova, A. Cartella, A. Cantaluppi, M. Först, D. Bossini, R. V. Mikheylovskiy, A. V. Kimel, R. Merlin, and A. Cavalleri, An effective magnetic field from optically driven phonons, *Nat. Phys.* **13**, 132 (2017).
- [75] D. M. Juraschek and N. A. Spaldin, Orbital magnetic moments of phonons, *Phys. Rev. Mater.* **3**, 064405 (2019).
- [76] M. Hamada, E. Minamitani, M. Hirayama, and S. Murakami, Phonon Angular Momentum Induced by the Temperature Gradient, *Phys. Rev. Lett.* **121**, 175301 (2018).
- [77] M. Hamada and S. Murakami, Phonon rotoelectric effect, *Phys. Rev. B* **101**, 144306 (2020).
- [78] K. Moseni, R. Wilson, and S. Coh, Electric field control of phonon angular momentum in perovskite $BaTiO_3$, [arXiv:2103.06316](https://arxiv.org/abs/2103.06316).
- [79] B. Cheng, T. Schumann, Y. Wang, X. Zhang, D. Barbalas, S. Stemmer, and N. P. Armitage, A large effective phonon magnetic moment in a Dirac semimetal, *Nano Lett.* **20**, 5991 (2020).
- [80] C. Xiao, Y. Ren, and B. Xiong, Adiabatically induced orbital magnetization, *Phys. Rev. B* **103**, 115432 (2021).

- [81] Y. Ren, C. Xiao, D. Saporov, and Q. Niu, Phonon magnetic moment from electronic topological magnetization, [arXiv:2103.05786](https://arxiv.org/abs/2103.05786).
- [82] W. R. Meier, M.-H. Du, S. Okamoto, N. Mohanta, A. F. May, M. A. McGuire, C. A. Bridges, G. D. Samolyuk, and B. C. Sales, Flat bands in the CoSn-type compounds, *Phys. Rev. B* **102**, 075148 (2020).
- [83] Z. Liu, M. Li, Q. Wang, G. Wang, C. Wen, K. Jiang, X. Lu, S. Yan, Y. Huang, D. Shen, J.-X. Yin, Z. Wang, Z. Yin, H. Lei, and S. Wang, Orbital-selective Dirac fermions and extremely flat bands in frustrated kagome-lattice metal CoSn, *Nat. Commun.* **11**, 4002 (2020).
- [84] P. E. Blöchl, Projector augmented-wave method, *Phys. Rev. B* **50**, 17953 (1994).
- [85] G. Kresse and J. Hafner, *Ab initio* molecular-dynamics simulation of the liquid-metal–amorphous-semiconductor transition in germanium, *Phys. Rev. B* **49**, 14251 (1994).
- [86] G. Kresse and J. Furthmüller, Efficient iterative schemes for *ab initio* total-energy calculations using a plane-wave basis set, *Phys. Rev. B* **54**, 11169 (1996).
- [87] G. Kresse and D. Joubert, From ultrasoft pseudopotentials to the projector augmented-wave method, *Phys. Rev. B* **59**, 1758 (1999).
- [88] J. P. Perdew, K. Burke, and M. Ernzerhof, Generalized Gradient Approximation Made Simple, *Phys. Rev. Lett.* **77**, 3865 (1996).
- [89] H. J. Monkhorst and J. D. Pack, Special points for Brillouin-zone integrations, *Phys. Rev. B* **13**, 5188 (1976).
- [90] T. Tadano, Y. Gohda, and S. Tsuneyuki, Anharmonic force constants extracted from first-principles molecular dynamics: applications to heat transfer simulations, *J. Phys.: Condens. Matter* **26**, 225402 (2014).
- [91] P. T. Jochym and J. Łażewski, High Efficiency Configuration Space Sampling—probing the distribution of available states, *SciPost Phys.* **10**, 129 (2021).
- [92] A. G. McLellan, Angular momentum states for phonons and a rotationally invariant development of lattice dynamics, *J. Phys. C: Solid State Phys.* **21**, 1177 (1988).
- [93] B. C. Sales, J. Yan, W. R. Meier, A. D. Christianson, S. Okamoto, and M. A. McGuire, Electronic, magnetic, and thermodynamic properties of the kagome layer compound FeSn, *Phys. Rev. Mater.* **3**, 114203 (2019).
- [94] B. C. Sales, W. R. Meier, A. F. May, J. Xing, J.-Q. Yan, S. Gao, Y. H. Liu, M. B. Stone, A. D. Christianson, Q. Zhang, and M. A. McGuire, Tuning the flat bands of the kagome metal CoSn with Fe, In, or Ni doping, *Phys. Rev. Mater.* **5**, 044202 (2021).
- [95] C. Zeng, P. R. C. Kent, M. Varela, M. Eisenbach, G. M. Stocks, M. Torija, J. Shen, and H. H. Weitering, Epitaxial Stabilization of Ferromagnetism in the Nanophase of FeGe, *Phys. Rev. Lett.* **96**, 127201 (2006).
- [96] J.-X. Yin, N. Shumiya, S. Mardanya, Q. Wang, S. S. Zhang, H.-J. Tien, D. Multer, Y. Jiang, G. Cheng, N. Yao, S. Wu, D. Wu, L. Deng, Z. Ye, R. He, G. Chang, Z. Liu, K. Jiang, Z. Wang, T. Neupert *et al.*, Fermion–boson many-body interplay in a frustrated kagome paramagnet, *Nat. Commun.* **11**, 4003 (2020).
- [97] See Supplemental Material at <http://link.aps.org/supplemental/10.1103/PhysRevB.104.054305> for visualizations of the chosen phonon modes. There, yellow (green) orbs correspond to the *p*-block (*d*-block) atoms. Files named `k_mode*` present modes from *K* point, while `gamma_mode4` correspond to the soft mode at Γ point in CoGe and RhPb.
- [98] G. Liu, Y. Jin, Z. Chen, and H. Xu, Straight nodal-line phonons in symmorphic space groups, *Phys. Rev. B* **104**, 024304 (2021).
- [99] Y. Tatsumi, T. Kaneko, and R. Saito, Conservation law of angular momentum in helicity-dependent Raman and Rayleigh scattering, *Phys. Rev. B* **97**, 195444 (2018).
- [100] H. Chen, W. Wu, J. Zhu, S. A. Yang, and L. Zhang, Propagating chiral phonons in three-dimensional materials, *Nano Lett.* **21**, 3060 (2021).
- [101] S. Coh, Classification of materials with phonon angular momentum and microscopic origin of angular momentum, [arXiv:1911.05064](https://arxiv.org/abs/1911.05064).
- [102] E. Solano-Carrillo, Chiral phonons and electrical resistivity of ferromagnetic metals at low temperatures, *Phys. Status Solidi B* **255**, 1800013 (2018).
- [103] C. Brendel, V. Peano, O. J. Painter, and F. Marquardt, Pseudomagnetic fields for sound at the nanoscale, *Proc. Natl. Acad. Sci. U.S.A.* **114**, E3390 (2017).
- [104] S. Zhang, N. Mao, N. Zhang, J. Wu, L. Tong, and J. Zhang, Anomalous polarized Raman scattering and large circular intensity differential in layered triclinic ReS₂, *ACS Nano* **11**, 10366 (2017).
- [105] S.-Y. Chen, C. Zheng, M. S. Fuhrer, and J. Yan, Helicity-resolved Raman scattering of MoS₂, MoSe₂, WS₂, and WSe₂ atomic layers, *Nano Lett.* **15**, 2526 (2015).
- [106] A. Rückriegel, S. Streib, G. E. W. Bauer, and R. A. Duine, Angular momentum conservation and phonon spin in magnetic insulators, *Phys. Rev. B* **101**, 104402 (2020).
- [107] M. Hamada and S. Murakami, Conversion between electron spin and microscopic atomic rotation, *Phys. Rev. Res.* **2**, 023275 (2020).
- [108] R. Sasaki, Y. Nii, and Y. Onose, Magnetization control by angular momentum transfer from surface acoustic wave to ferromagnetic spin moments, *Nat. Commun.* **12**, 2599 (2021).
- [109] G. Schaack, Observation of circularly polarized phonon states in an external magnetic field, *J. Phys. C: Solid State Phys.* **9**, L297 (1976).
- [110] D. M. Juraschek and P. Narang, Giant phonon-induced effective magnetic fields in 4*f* paramagnets, [arXiv:2007.10556](https://arxiv.org/abs/2007.10556).
- [111] Y. Zhang, Y.-W. Tan, H. L. Stormer, and P. Kim, Experimental observation of the quantum Hall effect and Berry's phase in graphene, *Nature (London)* **438**, 201 (2005).
- [112] S. Park and B.-J. Yang, Phonon angular momentum Hall effect, *Nano Lett.* **20**, 7694 (2020).
- [113] Y. Peng, B. Yan, J. Xie, E. Liu, H. Li, R. Ge, F. Gao, and J. Liu, Variation of topological edge states of 2D honeycomb lattice photonic crystals, *Phys. Status Solidi. Rapid Res. Lett.* **14**, 2000202 (2020).
- [114] L.-H. Wu and X. Hu, Scheme for Achieving a Topological Photonic Crystal by Using Dielectric Material, *Phys. Rev. Lett.* **114**, 223901 (2015).
- [115] K. Momma and F. Izumi, VESTA3 for three-dimensional visualization of crystal, volumetric and morphology data, *J. Appl. Crystallogr.* **44**, 1272 (2011).
- [116] W. Humphrey, A. Dalke, and K. Schulten, VMD: Visual molecular dynamics, *J. Mol. Graph.* **14**, 33 (1996).